J. Fluid Mech. (1991), *vol.* 224, *pp.* 49–76
Printed in Great Britain

Linear and nonlinear barotropic instability of geostrophic shear layers

By L. J. PRATT AND J. PEDLOSKY
Department of Physical Oceanography, Woods Hole Oceanographic Institution, Woods Hole, MA 02543, USA

(Received 30 March 1990 and in revised form 3 August 1990)

The linear, weakly nonlinear and strongly nonlinear evolution of unstable waves in a geostrophic shear layer is examined. In all cases, the growth of initially small-amplitude waves in the periodic domain causes the shear layer to break up into a series of eddies or pools. Pooling tends to be associated with waves having a significant varicose structure. Although the linear instability sets the scale for the pooling, the wave growth and evolution at moderate and large amplitudes is due entirely to nonlinear dynamics. Weakly nonlinear theory provides a catastrophic time t_s at which the wave amplitude is predicted to become infinite. This time gives a reasonable estimate of the time observed for pools to detach in numerical experiments with marginally unstable and rapidly growing waves.

1. Introduction

Studies of waves in oceanic fronts and jets have traditionally stressed sinuous (or meandering) modes of motion. This emphasis is due in part to observations of formation of mesoscale eddies through detachment of meander crests and troughs. Perhaps the best known example of eddy formation associated with meandering motions is Gulf Stream ring generation (Richardson 1983). Observations of these and related features have prompted study of 'thin jet' models (see Flierl & Robinson (1984), Pratt (1988), and references contained therein) in which restriction to sinuous mode behaviour is made by suppressing variations in cross-stream structure along the axis of the jet.

Recent attention has been drawn to features which exhibit varicose structure, i.e. *width* variations along the jet axis. One example is the warm outbreak (Cornillon, Evans & Large 1986), a detached eddy which originates from a bulge in the southern boundary of the stream. Also, varicose wave modes in idealized jets have been found instrumental in upstream influence and blocking (Pratt 1989; Armi 1989). Beyond their linear stability properties (Talley 1983*a*, *b*) little is known about the finite-amplitude behaviour of varicose modes in mid-latitude jets. Pratt *et al.* (1990, hereinafter referred to as PECC), attempted to clarify the dynamics of warm outbreak formation by studying the nonlinear steepening and breaking of mixed (sinuous–varicose) wave modes in an equivalent barotropic jet. By restricting attention to piecewise continuous potential vorticity, the authors were able to formulate a finite-amplitude long-wave theory giving the signal speeds of constant-width values for the jet. Smaller widths propagated more rapidly than larger widths giving rise to a nonlinear steepening phenomena. Numerical solutions based on the method of contour dynamics showed that the steeping waves could sometimes break and eject blobs of fluid resembling warm outbreaks. In addition to steepening, the

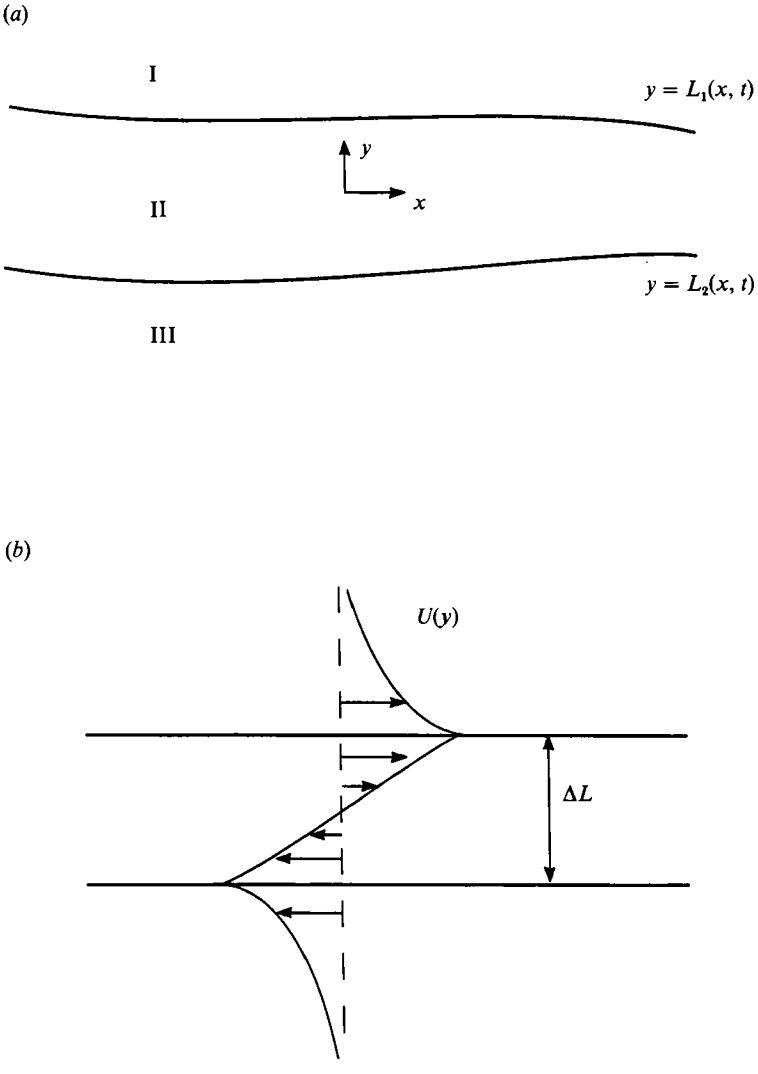

FIGURE 1. (*a*) Plan view of the active layer in the $1\frac{1}{2}$-layer model. The three regions (I, II, and III) of uniform potential vorticity and separated by potential vorticity fronts at $y = L_1$ and $y = L_2$. (*b*) Qualitative representation of the velocity profile for $L_1 = \text{constant}$, $L_2 = \text{constant}$, and $\Delta L = L_1 - L_2 = 1$.

outbreak formation also relied on a barotropic instability which amplified mixed waves modes generated during the steepening. The presence of both processes made a clear understanding of the dynamics difficult. In particular, it was not known whether the instability alone could produce detached eddies.

The purpose here is to gain a deeper understanding of the barotropic instability by treating it in isolation. We do so by considering a special case of the PECC jet for which nonlinear long-wave steepening is absent (all widths propagate at the same speed), a condition which can be created by imposing a particular potential vorticity distribution. Linear and weak nonlinear calculations (§§3 and 4) are made to determine properties of growing mixed waves, indicating possible space- and timescales for the eventual large-amplitude state. These calculations are supplemented by numerical solutions (§5) showing eddy formation. The eddy spacing

depends upon the mix of wavelengths present in the initial condition and is not necessarily determined by the length of the most rapidly growing linear wave; both the phase and growth rate properties determine the outcome. We will also show that the 'catastrophe' time (that required for eddies to begin detaching) can be approximated using weak nonlinear theory. Although the latter is formally valid only for marginally stable waves, the predicted catastrophe time remains approximately valid for rapidly growing waves as well. Finally, we show that once the unstable waves grow past an amplitude threshold, the subsequent evolution and growth is due entirely to nonlinear dynamics. This result is demonstrated by interrupting the numerical integration and 'linearly stabilizing' the solution, i.e. adjusting a lengthscale so as to make the corresponding basic state stable. Despite this artificial deformation, the flow continues to evolve in qualitatively the same manner as the uninterrupted flow.

The importance of the phase structure in determining eddy spacing, the success of weakly nonlinear theory in predicting the detachment time, and the insensitivity of the finite amplitude states to linear instability all have implications for forecasting of eddy detachment in the ocean.

The basic velocity profile of the model, a geostrophic shear layer or alternate jet, is shown in figure 1(*b*). The shear layer is a special case of more general jet-like profiles considered by PECC and is reminiscent of certain equatorial and deep northern Pacific (Warren & Owens 1988) flows. The focus on the special case is due to the absence of nonlinear long-wave steepening and the presence of symmetry properties which greatly simplify the (already arduous) weakly nonlinear calculation.

2. The model

Consider an equivalent barotropic, quasi-geostrophic flow on an f-plane. Denoting the mean thickness of the active (upper) layer by D, the actual thickness by $D+h$, the Coriolis parameter by f and the reduced gravity g', the quasi-geostrophic potential vorticity is given by $(g'/fD)\nabla^{*2}h^* - (f/D^2)h^*$. Let the latter have the constant values (f/D^2) $(0, -h_2^*, 0)$ within the regions I, II, and III shown in figure 1, so that

$$\left(\frac{g'D}{f^2}\right)\nabla^{*2}h^* - h^* = \begin{cases} 0 & (y^* > L_1^*), \\ -h_2^* & (L_1^* > y^* > L_2^*), \\ 0 & (y^* < L_2^*). \end{cases} \tag{2.1}$$

(Notice that $D+h_2^*$ is the region II layer thickness in the absence of relative vorticity.) The eastward and northward velocity components u^* and v^* are related to h^* by the geostrophic relations

$$fu^* = -g'h_{y^*}^*, \tag{2.2a}$$

$$fv^* = +g'h_{x^*}^*. \tag{2.2b}$$

Introducing the dimensionless variables

$$h = \frac{h^*}{h_2^*}, \qquad (x, y) = (x^*, y^*)\ \frac{f}{(g'D)^{\frac{1}{2}}}, \qquad (L_1, L_2) = (L_1^*, L_2^*)\frac{f}{(g'D)^{\frac{1}{2}}},$$

$$t = \frac{g'h_2^*}{f}, \quad (u, v) = (u^*, v^*)\ \frac{1}{h_2^*}\left(\frac{D}{g'}\right)^{\frac{1}{2}},$$

Equations (2.1) and (2.2) become

$$\nabla^2 h - h = \begin{cases} 0 & (y > L_1), \\ -1 & (L_1 > y > L_2), \\ 0 & (y < L_2), \end{cases} \tag{2.3}$$

$$u = -h_y, \tag{2.4a}$$

$$v = h_x. \tag{2.4b}$$

A simple example of a flow governed by (2.1) is the steady zonal state $h = H(y)$, $u = \mathscr{U}(y)$, and $v = 0$ occurring when $L_1 = -L_2 = \frac{1}{2}\Delta L = \text{constant}$. The solution having continuous h and u is

$$H(y) = U \begin{cases} \exp(-(y - \frac{1}{2}\Delta L)) & (y > \frac{1}{2}\Delta L), \\ U^{-1} - \dfrac{\cosh(y)}{\sinh(\frac{1}{2}\Delta L)} & (|y| < \frac{1}{2}\Delta L), \\ \exp(y + \frac{1}{2}\Delta L) & (y < -\frac{1}{2}\Delta L), \end{cases} \tag{2.5}$$

$$\mathscr{U}(y) = U \begin{cases} \exp(-(y - \frac{1}{2}\Delta L)) & (y > \frac{1}{2}\Delta L), \\ \dfrac{\sinh(y)}{\sinh(\frac{1}{2}\Delta L)} & (|y| < \frac{1}{2}\Delta L), \\ -\exp(y + \frac{1}{2}\Delta L) & (y < \frac{1}{2}\Delta L), \end{cases} \tag{2.6}$$

where

$$U = T/(1+T) = \tfrac{1}{2}(1 - e^{-\Delta L}), \tag{2.7}$$

and

$$T = \tanh(\tfrac{1}{2}\Delta L). \tag{2.8}$$

The velocity profile (drawn in figure 1*b* for $\Delta L = 1$) is antisymmetric, consisting of 'eastward'- and 'westward'-flowing cusped lobes with maximum speed U. In our scaled system of variables U depends only on the frontal separation ΔL, as shown by (2.7). However, the dimensional value

$$U^* = \frac{U g'^{\frac{1}{2}} h_2^*}{H^{\frac{1}{2}}} = \frac{g'^{\frac{1}{2}} h_2^* T}{H^{\frac{1}{2}}(1+T)}$$

is proportional to the potential vorticity jump h_2^*.

The flow described by (2.5)–(2.7) forms a basic state whose linear and weakly nonlinear instability will be examined. Also, we will wish to compute the large amplitude states which ultimately arise as a result of linear instability. The method of contour dynamics provides an algorithm for computing the evolution of $L_1(x,t)$ and $L_2(x,t)$ to large-amplitude, highly contorted configurations given the initial values $L_1(x,0)$ and $L_2(x,0)$. PECC have formulated the evolution equation for arbitrary (but constant) values of the potential vorticity in regions I, II, and III, and the equations governing the present case, obtained by setting the potential vorticity jump ratio (their r) to unity, are

$$\frac{dx_1}{dt} = \int_{-\infty}^{\infty} G[x, L_1(x); \xi_2, L_2(\xi_2)]\, d\xi_2 - \int_{-\infty}^{\infty} G[x, L_1(x); \xi_1, L_1(\xi_1)]\, d\xi_1, \tag{2.9a}$$

$$\frac{dL_1}{dt} = \int_{L_2(-\infty)}^{L_2(\infty)} G[x, L_1(x); \xi_2, L_2(\xi_2)]\, dL_2 - \int_{L_1(-\infty)}^{L_1(\infty)} G[x, L_1(x); \xi_1, L_1(\xi_1)]\, dL_1, \tag{2.9b}$$

$$\frac{dx_2}{dt} = \int_{-\infty}^{\infty} G[x, L_2(x); \xi_2, L_2(\xi_2)]\, d\xi_2 - \int_{-\infty}^{\infty} G[x, L_2(x); \xi_1, L_1(\xi_1)]\, d\xi_1, \tag{2.9c}$$

$$\frac{dL_2}{dt} = \int_{L_2(-\infty)}^{L_2(-\infty)} G[x, L_2(x); \xi_2, L_2(\xi_2)]\, dL_2 - \int_{L_1(\infty)}^{L_1(\infty)} G[x, L_2(x); \xi_1, L_1(\xi_1)]\, dL_1, \tag{2.9d}$$

where $$G(x, y; \xi, \eta) = \frac{-1}{2\pi} K_0[(x-\xi)^2 + (y-\eta)^2]^{\frac{1}{2}},$$

and K_0 denotes the modified Bessel function of zero order. Here (x_n, L_n) represents the position of a fluid parcel on the northern ($n = 1$) or southern ($n = 2$) front and $\mathrm{d}/\mathrm{d}t$ the Lagrangian derivative. The integrations are carried out along each contour, with $\mathrm{d}\xi_n$ and $\mathrm{d}L(\xi_n)$ representing differential increments in x and y. The equations can be solved by resolving each front using a finite number of Lagrangian points, evaluating the contour integrals numerically, and employing a time-stepping scheme. The procedure of PECC is employed here with adjustments to accommodate periodic boundary conditions, as described in Appendix A. The contours (fronts) are allowed to become multi-valued with respect to x, but not to break. More sophisticated routines employing higher-order integration schemes and contour surgery are available and the reader is referred to Zabusky & Overman (1981) and Dritschel (1988), and references contained therein for further details.

In the development of the contour dynamical formulation, it is assumed the velocity is continuous across each front. Continuity of h (essentially the pressure) along with the geostrophic relations assures continuity of the velocity normal to the front. Continuity of the tangential velocity component is assured by the specification of piecewise continuous potential vorticity; discontinuities in the tangential velocity would imply delta function behaviour in the potential vorticity. Pedlosky (1990) discusses the matching condition at a potential vorticity front when the tangential velocity is allowed to be discontinuous. It is shown that the jump in tangential velocity remains zero if it is initially zero. In summary, our continuous velocity assumption is based on the continuity of h and on the assumption that (i) the potential vorticity remains bounded, or (ii) all motions originate from a state of continuous tangential velocity.

3. Linear stability analyses

Consider small departures from the basic state (2.5)–(2.7) by writing

$$h = H(y) + \epsilon[\phi^{(0)}(x, y, t) + \epsilon\phi^{(1)}(x, y, t) + \ldots], \tag{3.1}$$

$$u = \mathscr{U}(y) - \epsilon[\phi_y^{(0)}(x, y, t) + \epsilon\phi_y^{(1)}(x, y, t) + \ldots], \tag{3.2}$$

$$v = \epsilon[\phi_x^{(0)}(x, y, t) + \epsilon\phi_x^{(1)}(x, y, t) + \ldots], \tag{3.3}$$

$$L_1 = \tfrac{1}{2}\Delta L + \epsilon[\eta_1^{(0)}(x, t) + \epsilon\eta_1^{(1)}(x, t) + \ldots], \tag{3.4}$$

$$L_2 = -\tfrac{1}{2}\Delta L + \epsilon[\eta_2^{(0)}(x, t) + \epsilon\eta_2^{(1)}(x, t) + \ldots]. \tag{3.5}$$

To $O(\epsilon)$ the field equation (2.3) becomes

$$\nabla^2\phi^{(0)} - \phi^{(0)} = 0. \tag{3.6}$$

At $y = L_1$ and $y = L_2$, continuity of h and u are imposed. These matching conditions are referenced to the undisturbed frontal positions through Taylor expansion of h and u about $y = \pm\frac{1}{2}\Delta L$. At $y = \frac{1}{2}\Delta L$, for example,

$$\begin{aligned} h = {} & H(\tfrac{1}{2}\Delta L) + \epsilon\eta_1 H_y(\tfrac{1}{2}\Delta L) + \tfrac{1}{2}\epsilon^2\eta_1^2 h_{yy}(\tfrac{1}{2}\Delta L) + \ldots \\ & + \epsilon[\phi^{(0)}(x, \tfrac{1}{2}\Delta L, t) + \epsilon\eta_1\phi_y^{(0)}(x, \tfrac{1}{2}\Delta L, t) + \tfrac{1}{2}\epsilon^2\eta_1^2\phi_{yy}^{(0)}(x, \tfrac{1}{2}\Delta L, t) + \ldots] \\ & + \epsilon^2[\phi^{(1)}(x, \tfrac{1}{2}\Delta L, t) + \epsilon\eta_1\phi_y^{(1)}(x, \tfrac{1}{2}\Delta L, t) + \ldots] \\ & + \ldots \end{aligned} \tag{3.7}$$

where $$\eta_n = \eta_n^{(0)}(x,t) + \epsilon\eta_n^{(1)}(x,t) + \epsilon^2\eta_n^{(2)}(x,t) + \ldots \tag{3.8}$$

To $O(\epsilon)$ the matching of h and u can be expressed

$$\delta[\phi^{(0)}] = 0 \quad (y = \pm\tfrac{1}{2}\Delta L), \tag{3.9a, b}$$

$$\delta[\phi_y^{(0)}] - \eta^{(0)}\,\delta[\mathscr{U}_y^{(0)}] = 0 \quad (y = \pm\tfrac{1}{2}\Delta L), \tag{3.10a, b}$$

where $\delta[F]$ denotes the north-to-south jump in F across the indicated value of y:

$$\delta[F] = \lim_{\alpha\to 0}[F(x, y+\alpha, t) - F(x, y-\alpha, t)].$$

In addition, L_n and h are related by the kinematic condition

$$\left(\frac{\partial}{\partial x}\right)h(x, L_n, t) = \left(\frac{\partial}{\partial t} + u(x, L_n, t)\frac{\partial}{\partial y}\right)L_n(x,t) \quad (n = 1, 2). \tag{3.11}$$

When the dependent variables are expanded as above, the $O(\epsilon)$ approximations to (3.11) at each front are

$$\frac{\partial\phi^{(0)}}{\partial x}(x, \tfrac{1}{2}\Delta L, t) = \left(\frac{\partial}{\partial t} + \mathscr{U}(\tfrac{1}{2}\Delta L)\frac{\partial}{\partial x}\right)\eta_1^{(0)}, \tag{3.12a}$$

$$\frac{\partial\phi^{(0)}}{\partial x}(x, -\tfrac{1}{2}\Delta L, t) = \left(\frac{\partial}{\partial t} + \mathscr{U}(-\tfrac{1}{2}\Delta L)\frac{\partial}{\partial x}\right)\eta_2^{(0)}. \tag{3.12b}$$

The linear-stability problem consists of seeking solutions to (3.6) of the form

$$\phi^{(0)} = \Phi(y)\,e^{ik(x-ct)} + *, \tag{3.13}$$

$$\eta_n^{(0)} = a_0 N_n^{(0)}\,e^{ik(x-ct)} + * \quad (n = 1, 2), \tag{3.14}$$

where $*$ denotes the complex conjugate of the preceding expression.

Substitution of (3.13) into (3.6) leads to

$$\frac{\partial}{\partial y^2}\Phi - \mu^2\Phi = 0,$$

where $\mu^2 = 1 + k^2$. The solution satisfying the matching conditions (3.9a, b), (3.10b, and (3.12a, b) is

$$\Phi(y) = \frac{a^{(0)}}{\gamma}\begin{cases}\gamma\exp(-\mu(y-\tfrac{1}{2}\Delta L)) & (y > \tfrac{1}{2}\Delta L),\\ [2\mu(U+c)-1]\exp(\mu(y-\tfrac{1}{2}\Delta L)) - \exp(-\mu\Delta L)\exp-(y+\tfrac{1}{2}\Delta L) & (|y| < \tfrac{1}{2}\Delta L),\\ 2\mu(U+c)\exp(-\mu\Delta L)\exp\mu(y+\tfrac{1}{2}\Delta L) & (y < -\tfrac{1}{2}\Delta L),\end{cases} \tag{3.15}$$

where $$\gamma = 2\mu(U+c) - 1 + \exp(-2\mu\Delta L),$$

and $$N_1 = (U-c)^{-1}, \tag{3.16}$$

$$N_2 = -2\mu\gamma^{-1}\exp(-\mu\Delta L). \tag{3.17}$$

The phase speed c can be obtained by substituting (3.15)–(3.17) into (3.10a) with the result

$$c^2 = \left(U - \frac{1}{2\mu}\right)^2 - \exp(-2\mu\Delta L). \tag{3.18}$$

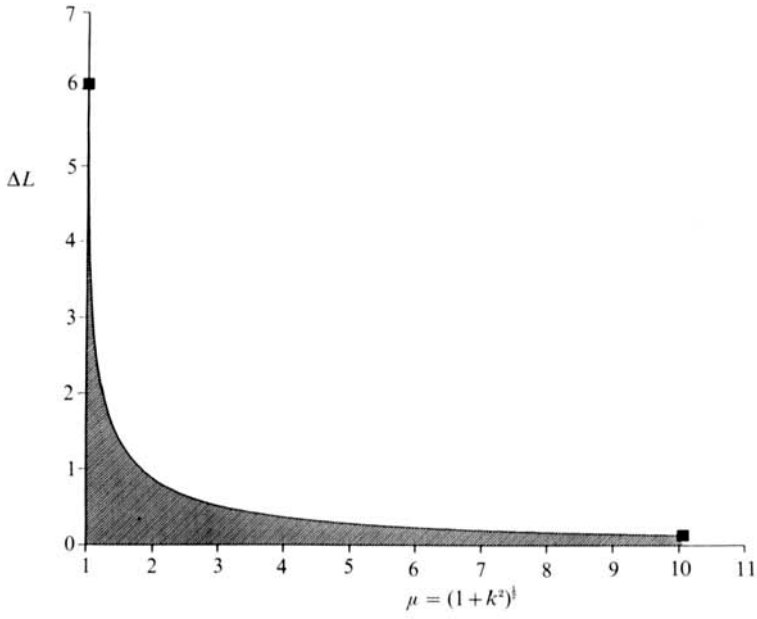

FIGURE 2. Stability diagram with the shaded region representing unstable values of ΔL and $\mu = (1+k^2)^{\frac{1}{2}}$.

For $U-(1/2\mu) < \exp(-2\mu\,\Delta L)$, c is pure imaginary, the solutions are stationary and exponentially growing in time. Using $U = \frac{1}{2}(1-\exp(-\Delta L))$, the neutral boundary is given by

$$1-\exp(-\Delta L) = \mu^{-1}(1+\exp(-\mu\,\Delta L). \tag{3.19}$$

Figure 2 shows a plot of the stability boundary in $(\mu, \Delta L)$-space as given by (3.19). The shaded area indicates unstable waves. For fixed ΔL, the instability occurs in a band extending from $\mu = 1$ (long waves) to a value $\mu > 1$. The width of this band decreases as ΔL increases; as the distance between fronts increases, the wavelength must increase in order that the growing modes sense both fronts. As $\Delta L \to 0$, the bandwidth becomes infinite. Figure 3 shows a typical growth rate curve (kc_i *vs.* μ) exhibiting marginally stable longwaves ($kc_i \to 0$ as $k \to 0$) and a short-wave cutoff.

The phase shift between fronts for an unstable wave varies with the wavenumber. For long waves ($\mu = 1$, $c = 0$) equations (3.16) and (3.17) reduce to

$$N_1 = N_2 = \frac{1}{U},$$

indicating zero phase lag. Long waves therefore have a sinuous structure. At the short-wave cutoff, it can easily be shown using (3.18) that (3.16) and (3.7) reduce to

$$N_1 = -N_2 = \frac{1}{U},$$

so that the two fronts are phase lagged by 180°. Marginally stable waves at the short-wave cutoff therefore have a symmetric or varicose structure. As μ varies from unity to its cutoff value, the crests of the south front lag those of the north front by an amount increasing from zero to 180°. A few sample values of phase lag have been

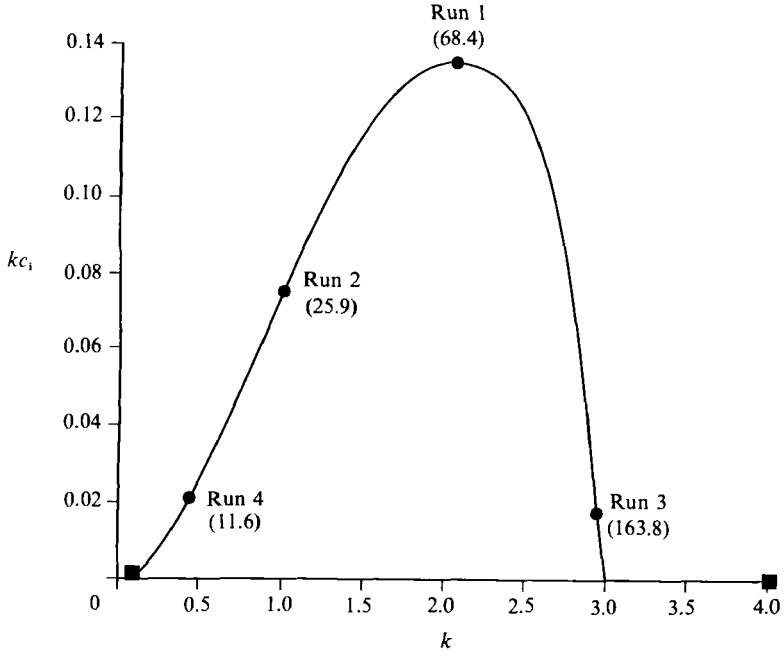

FIGURE 3. Growth rate curve for $\Delta L = 0.5$. The k and kc_i values for the primary wave used in the numerical experiments are indicated along with the corresponding values of the phase lag θ_1.

labelled on the figure 3 growth rate curve, and the most unstable wave clearly has a mixed (sinuous/varicose) structure. Griffiths, Killworth & Stern (1981) found a similar phase structure in connection with ageostrophic instabilities of gravity currents.

We note that the stationarity of long waves ($c = 0$) is a result that can be extended to arbitrary large amplitude [see equation (3.8) in PECC]. The implication is that any initial disturbance having gradual but large variations in L_1 and L_2 remains stationary; no nonlinear steepening occurs. This result holds true only when the potential vorticity in regions I and III are identical.

The symmetrical mode at the short-wave cutoff is central to our subsequent nonlinear analysis. Its structure is described by

$$\Phi^{(0)} = a_0 \exp(ikx) \begin{cases} \exp(-\mu(y-\tfrac{1}{2}\Delta L)) & (y > \tfrac{1}{2}\Delta L), \\ \dfrac{\cosh \mu y}{\cosh(\tfrac{1}{2}\mu \Delta L)} + * & (|y| < \tfrac{1}{2}\Delta L), \\ \exp(\mu(y+\tfrac{1}{2}\Delta L)) & (y < -\tfrac{1}{2}\Delta L), \end{cases} \tag{3.20}$$

$$N_1 = \frac{a_0 e^{ikx}}{U} + *, \tag{3.21}$$

$$N_2 = \frac{-a_0 e^{ikx}}{U} + *. \tag{3.22}$$

4. Weakly nonlinear theory

The disturbance described in the previous section will continue to grow exponentially until, at finite amplitude, the nonlinear interactions can no longer be ignored. In the present problem, the potential vorticity is uniform in each region which eliminates wave–mean flow interactions. The interaction which occurs is a wave–wave interaction. The growing wave first self-interacts producing a spatial second harmonic which subsequently reacts with the primary wave to affect its growth. In order to ascertain whether this interaction is stabilizing or further destabilizing, we first consider a weakly nonlinear theory for the evolution. It is simplest to imagine the problem formulated in the following way.

Consider an initial disturbance with wavenumber k. Fix the dimensional width of the shear zone,

$$\Delta L^* = L_1^* - L_2^*. \tag{4.1}$$

The we choose the deformation radius $L_D = (g'D)^{\frac{1}{2}}/f$ to be such that

$$\kappa \equiv \frac{\frac{1}{2}\Delta L^*}{L_D} = \tfrac{1}{2}\Delta L \tag{4.2}$$

is slightly in excess of that value $\kappa_0 = (\frac{1}{2}\Delta L)_0$ for which (3.19) is just satisfied. For

$$\kappa = \kappa_0 + \delta\kappa, \quad \delta\kappa \ll \kappa, \tag{4.3}$$

the wave will grow slowly enough that a perturbation expansion pivoted about the neutral solution that obtains when $\delta\kappa = 0$ can be constructed in which the time development of the wave amplitude is balanced by both the linear destabilization of $O(\delta\kappa)$ and the nonlinearity of $O(\epsilon^2)$. In the more realistic parameter settings discussed in the following sections a much broader spectrum of waves may grow. We emphasize that the present restrictive setting is chosen so that we may analytically investigate in a concrete fashion the role of nonlinearity in the wave development. Of course, the parameter setting described by (4.3) is certainly a consistent if restrictive one. Introducing a rescaled time

$$T = \epsilon t, \tag{4.4}$$

we choose

$$\epsilon = (\delta\kappa)^{\frac{1}{2}}. \tag{4.5}$$

For the purposes of the perturbation series, it is useful to scale x^* and y^* with $\frac{1}{2}\Delta L^*$ so that the width of the shear zone in non-dimensional units always runs between

$$-1 \leqslant \tilde{y} \leqslant 1,$$

where $\tilde{y} = 2y^*/\Delta L^* = (2/\Delta L)\, y$. This means that as

$$\kappa = \tfrac{1}{2}\Delta L \tag{4.6}$$

is perturbed, the non-dimensional width of the shear zone in the y variable is perturbed since L_D is changed. In the $\tilde{y}$ variable, the width is fixed.

In each region

$$\nabla^2\phi - \kappa^2\phi = 0, \tag{4.7}$$

where now $\nabla^2 \equiv \partial^2/\partial\tilde{y}^2 + \partial^2/\partial x^2$, while

$$\kappa^2 \sim \kappa_0^2 + 2\kappa_0\,\delta\kappa. \tag{4.8}$$

Continuity of each velocity component at the perturbed shear zone boundary implies that, i.e. at the upper boundary

$$\frac{\partial\phi}{\partial x}(x, 1+\epsilon\eta) = \frac{\partial\phi}{\partial x}(x, 1) + \epsilon\frac{\partial^2\phi}{\partial x\partial\tilde{y}}\eta + \epsilon^2\frac{\partial^3\phi}{\partial x\partial\tilde{y}^2}\frac{\eta^2}{2} + \ldots \tag{4.9}$$

is continuous, while for the zonal velocity we require the continuity of

$$\mathscr{U}(1+\epsilon\eta) - \epsilon\frac{\partial\phi}{\partial y} = \mathscr{U}(1) + \epsilon\frac{\partial\mathscr{U}}{\partial\tilde{y}}\eta + \epsilon^2\frac{\partial^2\mathscr{U}}{\partial\tilde{y}^2}\frac{\eta^2}{2} + \ldots - \epsilon\frac{\partial\phi}{\partial y} - \epsilon^2\frac{\partial^2\phi}{\partial y^2}\eta - \ldots. \tag{4.10}$$

Each variable on the right-hand sides of (4.9) and (4.10) is evaluated at $\tilde{y} = 1$. Similar continuity conditions are imposed at $\tilde{y} = -1$.

The shear zone boundaries are calculated from the kinematic condition, i.e. at the upper frontal boundary

$$\epsilon\frac{\partial\eta}{\partial T} + u\frac{\partial\eta}{\partial x} = \frac{\partial\phi}{\partial x} \quad \text{at } \tilde{y} = 1+\epsilon\eta, \tag{4.11}$$

whose Taylor series expansion, similar to (4.9) and (4.10) allows a sequence of problems to be formulated in which the η, ϕ relation is remapped to $\tilde{y} = 1$.

The basic flow $\mathscr{U}(\tilde{y})$, noting the relation between $\tilde{y}$ and y is,

$$\mathscr{U}(\tilde{y}) = U\begin{cases} \exp(-\kappa(\tilde{y}-1)) & (\tilde{y} > 1), \\ \dfrac{\sinh(\kappa\tilde{y})}{\sinh\kappa} & (-1 \leqslant \tilde{y} \leqslant 1), \\ -\exp(\kappa(\tilde{y}+1)) & (\tilde{y} < -1), \end{cases} \tag{4.12}$$

(cf. equation (2.6)). Note that at $\tilde{y} = 1$, for example

$$\frac{\mathrm{d}\mathscr{U}}{\mathrm{d}\tilde{y}} = U\begin{cases} -\kappa & \tilde{y} = 1_+, \\ \kappa\coth\kappa & \tilde{y} = 1_-, \end{cases} \tag{4.13}$$

so that the basic flow shear, which figures in the continuity requirement (4.10), will also have a κ expansion.

If ϕ and η are expanded in a series in ϵ as in (3.1), (3.4) and (3.5) and the expansions are inserted into (4.7), (4.9), (4.10) and (4.11) (and their equivalents at $\tilde{y} = -1$), a sequence of linear problems obtains. With attention to the ordering relation $\epsilon^2 = O(\delta\kappa)$, the results of this problem sequence is as follows. At lowest order, the marginal wave with $\kappa = \kappa_0$ is obtained, viz. in terms of $\tilde{y}$

$$\phi^{(0)} = A(T)\exp(\mathrm{i}kx)\begin{cases} \exp(-\mu(\tilde{y}-1)) & (\tilde{y} \geqslant 1), \\ \dfrac{\cosh\mu(\tilde{y})}{\cosh\mu} & +* \quad (|\tilde{y}| \leqslant 1), \\ \exp(\mu(\tilde{y}+1)) & (\tilde{y} \leqslant -1), \end{cases} \tag{4.14}$$

where now

$$\mu^2 = \kappa^2 + \kappa_0^2. \tag{4.15}$$

The parameter μ is further related to κ_0 by the condition that the wave, to lowest order be neutral, i.e. that k be related to $\frac{1}{2}\Delta L$ (or κ) by (3.19). In current variables, this is equivalent to

$$\mu(1+\tanh\mu) = \kappa_0(1+\coth\kappa_0). \tag{4.16}$$

The key feature of the analysis is that the amplitude, instead of being constant is an as yet unspecified function of the slow growth time T. The weakly nonlinear theory provides an evolution equation for the *amplitude* of $\phi^{(0)}$ while its spatial structure is given by that of the marginal wave.

A straightforward consideration of the higher-order problems yields the following results. The next correction to the perturbation stream function is:

$$\phi^{(1)} = \begin{cases} B\exp(-\mu(\tilde{y}-1))\exp(ikx) + D_a\exp(2ikx)\exp(-\gamma(\tilde{y}-1)) & (\tilde{y}>1), \\ B\dfrac{\sinh\mu\tilde{y}}{\sinh\mu}\exp(ikx) + D_b\exp(2ikx)\dfrac{\cosh\gamma\tilde{y}}{\cosh\gamma} + * & (|\tilde{y}|\leqslant 1), \\ -B\exp(\mu(y-1))\exp(ikx) - D_a\exp(2iks)\exp(\gamma(\tilde{y}+1)) & (\tilde{y}<-1), \end{cases} \tag{4.17}$$

where $\gamma = (4k^2+\kappa_0^2)^{\frac{1}{2}}$ and where

$$B(T) = -\frac{c^{\mu}\sinh\mu}{\mathscr{U}ik}\frac{dA}{dT}, \tag{4.18a}$$

$$D_b(T) = \frac{A^2}{2\mathscr{U}}\frac{\left[\dfrac{\mu^2}{\cosh^2\mu} - \kappa_0(\kappa_0-\gamma)(1+\coth\kappa_0)\right]}{\kappa_0(1+\coth\kappa_0)-\gamma(1+\tanh\gamma)}, \tag{4.18b}$$

$$D_a(T) = D_b + \frac{\kappa_0(1+\coth\kappa_0)A^2}{2\mathscr{U}}. \tag{4.18c}$$

This correction involves first a portion with the same wavenumber, k, as the primary wave but phase-shifted in $\tilde{y}$. This phase shift is proportional to the *rate of change* of A. The second part of $\phi^{(1)}$ is the double-harmonic solution directly forced by the amplitude of the primary wave.

When the problem is carried to next order, the interaction of the $\phi^{(0)}$ and $\phi^{(1)}$ solutions will produce forcing terms which would project resonantly on the linear operator for which $\phi^{(0)}$ is a solution. To render the ϵ expansion valid, the terms which resonate with the linear operator must be constrained by insisting that they be orthogonal to the appropriate adjoint operator. Again, the details of the solution are straightforward and are omitted. The resulting constraint yields the amplitude equation for $A(T)$, namely

$$\frac{d^2A}{dT^2} + k^2\frac{\delta\kappa}{\epsilon^2}U^2C_1A + k^2C_2A|A|^2 = 0, \tag{4.19}$$

where the constants C_1 and C_2 are given in Appendix B. The constant C_1 is related directly to the (imaginary) phase speed that obtains for slightly supercritical values of κ. The value of $\delta\kappa C_1$ is, of course, negative. The important consequence of the weakly nonlinear calculation is the sign of C_2. As shown in figure 4, C_2 is negative for all values of $\kappa\,(=\frac{1}{2}\Delta L)$ implying that the effect of the wave–wave interaction involving the double harmonic of the fundamental is destabilizing. According to weakly nonlinear theory, the effects of nonlinearity are to accelerate the growth of the perturbation. Indeed, according to (4.19) at some finite time, T_s, the amplitude becomes infinite. It is important to note that weakly nonlinear theory remains valid, although $C_2<0$, until the 'catastrophe' time, T_s. The rate at which the solution approaches the singularity occurring at that time remains consistent with the scaling (4.5). The singularity is only 'explosive' on the slow timescale. By then the

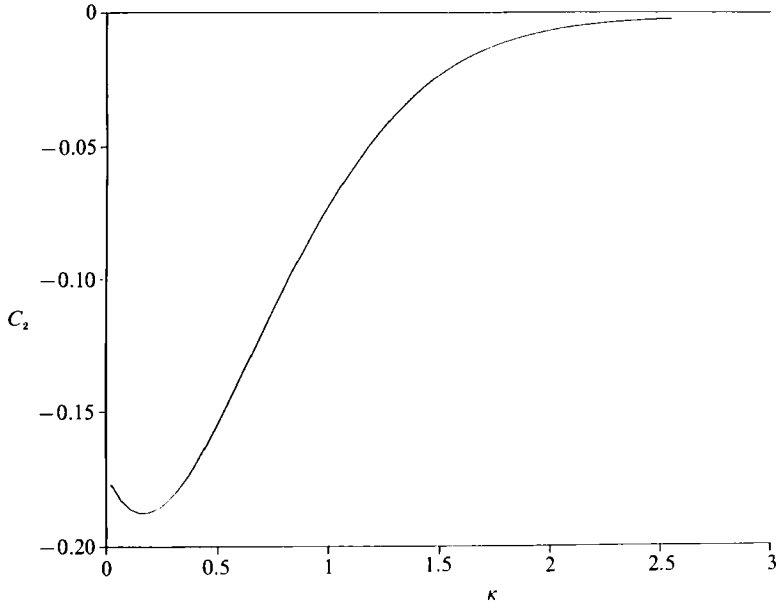

FIGURE 4. Plot of C_2 as a function of $\kappa = \frac{1}{2}\Delta L$.

perturbation scheme on which (4.19) is based becomes invalid, but it is interesting in light of our numerical calculations reported below to calculate T_s.

Let
$$\tau = \sigma\left(\frac{T}{\epsilon}\right), \tag{4.20a}$$

$$A = \frac{\sigma}{\epsilon k(-C_2)^{\frac{1}{2}}}\Theta, \tag{4.20b}$$

where σ is the linear growth rate, in the original units of time, i.e.

$$\sigma = kU(-\delta\kappa C_1)^{\frac{1}{2}}, \tag{4.21}$$

and the amplitude is measured in units such that the amplitude equation becomes

$$\frac{\mathrm{d}^2\Theta}{\mathrm{d}t^2} = \Theta + \Theta^3. \tag{4.22}$$

If (4.22) is solved subject to the particular initial condition

$$\left.\begin{aligned}\Theta &= \Theta_0\\ \frac{\mathrm{d}\Theta}{\mathrm{d}\tau} &= \Theta_0\end{aligned}\right\} \quad t = 0, \tag{4.23}$$

we are then following the evolution of the solution which at small amplitude consists solely of an exponentially growing wave with the linear e-folding rate, i.e. for small t, assuming $\Theta_0 \ll 1$, the solution for Θ will go like $\Theta_0 \mathrm{e}^{\tau}$. The solution to (4.22) and all subsequent time can be found in terms of elliptic functions. The principal result of interest is the time τ_s for which Θ becomes infinite. We find

$$\tau_s = \frac{1}{\{1+\frac{1}{4}\Theta_0^4\}^{\frac{1}{2}}} F(\alpha_0, m), \tag{4.24}$$

where F is the normal elliptic integral of the first kind (Byrd & Friedman 1971). The modulus m satisfies

$$m^2 = \frac{1+(1+\frac{1}{4}\Theta_0^4)^{\frac{1}{2}}}{2(1+\frac{1}{4}\Theta_0^4)^{\frac{1}{2}}}, \tag{4.25}$$

while the argument α_0 is given by the relation

$$\sin\alpha_0 = \left[\frac{2(1+\frac{1}{4}\Theta_0^4)^{\frac{1}{2}}}{1+\Theta_0^2+(1+\frac{1}{4}\Theta_0^4)^{\frac{1}{2}}}\right]^{\frac{1}{2}}. \tag{4.26}$$

If we consider the interesting limit where the initial condition is small enough so that initially the nonlinear terms are negligible, i.e. for $\theta_0 \ll 1$, we may easily find τ_s. For example, if $\Theta_0 = 0.1$, then $m = 0.9999969$, $\alpha_0 = 84.26°$ and $F(\alpha_0, m) \sim 3.1$ leading to

$$t_s = \frac{T_s}{\epsilon} = \frac{\tau_s}{\sigma} = \frac{3.1}{\sigma}. \tag{4.27}$$

The time required for the solution to explosively reach large amplitude is thus about three linear e-folding times. The catastrophe of infinite amplitude in a finite time is entirely a nonlinear effect. Its occurrence in weakly nonlinear theory is a hint of what we shall subsequently observe numerically, i.e. that the development of large pooled vortices is due fundamentally to the nonlinear development dynamics while the linear instability serves mainly to sow the seed perturbations from which the vortices emerge by nonlinear interactions

5. Numerical results

Table 1 lists the vital statistics for each numerical experiment, including the initial conditions and information on numerical resolution. The majority of experiments were carried out using $\Delta L = 0.5$, with a smaller number using $\Delta L = 0.25$ and $\Delta L = 0.75$. The growth rate curve for $\Delta L = 0.5$ (figure 3) shows a maximum value of kc_i at $k \approx 2.0$ and a short-wave cutoff at $k \approx 3.0$. Initial conditions typically involve combinations of the most unstable wave ($k \approx 2.0$), its subharmonics ($k \approx 1.0$, 0.5, etc.) and a marginally unstable wave ($k = 2.9$). The domain of the numerical solution extends over one primary wavelength.

5.1. *The most unstable wave* ($k = 2$)

Consider the initial condition

$$L_1 = \tfrac{1}{2}\Delta L + 0.02\sin(kx), \tag{5.1a}$$

$$L_2 = -\tfrac{1}{2}\Delta L + 0.02\sin(kx+\theta_1), \tag{5.1b}$$

with $\Delta L = 0.5$, $k = 2.0$, and $\theta_1 = 1.19$. These settings (labelled Run 1 in table 1) correspond to a small-amplitude wave having the maximum growth rate (an e-folding time $1/kc_i = 7.34$).

Figure 5 shows the evolution of the flow, with the shaded area representing fluid between the potential vorticity fronts. As a visual aid, two wavelengths of the periodic domain are shown. The lowest frame ($t = 7.34$) shows the flow after one e-folding time. The wave is structurally similar to the initial condition (not shown) with the wave crests L_2 lagging those of L_1. The amplitude of each front has increased from 0.02 to 0.053, which corresponds to a growth rate only 2% less than predicted by linear theory.

Run	ΔL	k	θ_0	NP	dt	t_e	t_p	t_s	Comments
1	0.5	2.0	1.19	20	0.367	7.34	30 ± 4	30.1	
2	0.5	1.0	0.45	40	0.750	13.15	57 ± 2	55.2	
2a	0.5	1.0	0.45	40	0.750	13.15	42 ± 2	41.2	Initial amplitude increased from 0.02 to 0.06.
2b	0.5	1.0	0.45	40	0.750	13.15	42 ± 2	55.2	Run interrupted at $t = 30$ and L_1 and L_2 increased to $4L_1$ and $4L_2$.
2c	0.5	2.0	0.45	60	0.5	13.15	75 ± 3	55.2	Higher resolution repeat of run 2.
2d	0.5	2.0	0.45	80	0.5	13.15	60 ± 5	72.1	Initial amplitude reduced from 0.02 to 0.005.
3	0.5	2.9	2.86	21	0.7	34.8	84 ± 8	94.0	Initial k close to shortwave cutoff 3.0.
3a	0.5	2.9	2.86	21	0.7	34.8	∞	94.0	At $t = 42$ run interrupted and L_1 and L_2 increased to $1.04\,L_1$ and $1.04\,L_2$; no pinch-off occurred.
3b	0.5	2.9	2.86	21	0.7	34.8	∞	94.0	Same as run 3a but interruption occurred at $t = 56$.
3c	0.5	2.9	2.86	40	0.7	34.8	63 ± 4	94.0	Same as run 3 but double resolution.
3d	0.5	2.9	2.86	40	0.7	34.8	70 ± 5	94.0	Same as run 3a but resolution doubled.
4	0.5	0.5	0.2	80	0.75	38.9	105 ± 5	120.6	
5	0.5	2.62	2.00	80	0.50	9.54	30 ± 3	29.6	Competition experiment using the two waves indicated.
and		1.31	0.642			9.54			
5a	0.5			80	0.50		30 ± 3	29.6	Same as run 5 but the shorter wave phase shifted by amount π in x-direction.
6	0.25	3.70	1.16	20	0.3	5.88	18 ± 3	18.2	
7	0.75	1.50	1.38	20	0.5	9.44	35 ± 3	34.9	

TABLE 1. Compilation of initial conditions (ΔL, k_1, and θ_0), number of nodes (NP) per wavelength, and timestep (dt) for each run. The initial condition takes the form

$$L_1 = \tfrac{1}{2}\Delta L + 0.02\sin(kx)$$
$$L_2 = -\tfrac{1}{2}\Delta L + 0.02\sin(kx+\theta_0)$$

unless otherwise indicated. Also shown are the e-folding time ($t_e = 1/kc_i$) for the primary wave, the observed pinch-off time t_p and the catastrophe time t_s.

At $t = 22.02$ (three e-folding times) the shaded fluid has begun to pool and by $t = 26.42$, the pools or eddies are roughly elliptical and rotate clockwise. Their spacing is equal to the primary wavelength, although their semi-major and semi-minor axes are shorter. The eddies are connected by filaments or strands across which the tangential velocity remains continuous. At $t = 33.76$, the convecting filaments contain virtually no mass and could probably be 'erased' with no serious dynamical

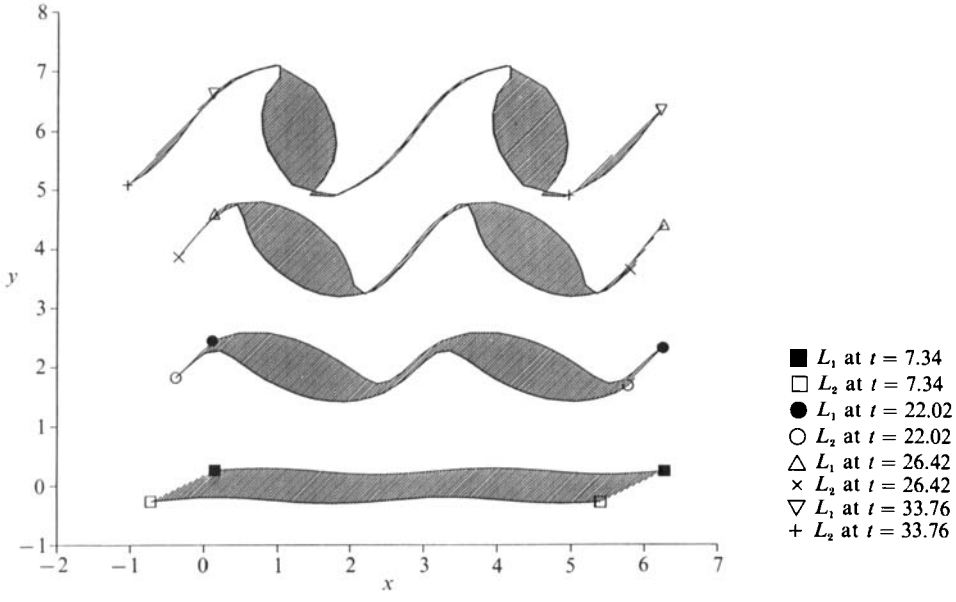

FIGURE 5. Run 1: $\Delta L = 0.5$, $k = 2.0$ (the linearly most unstable waves). Two periods are shown.

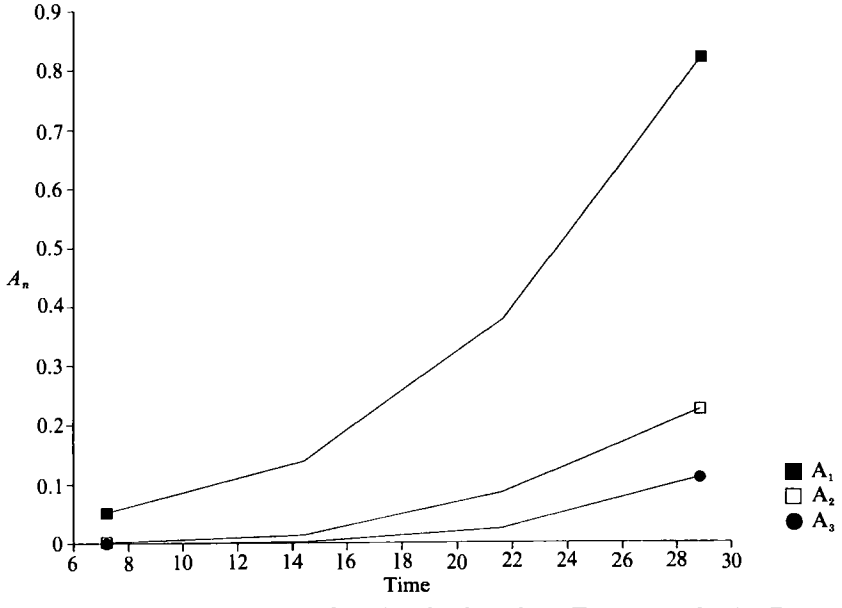

FIGURE 6. Amplitudes A_1, A_2, and A_3 for the first three Fourier modes for Run 1.

consequences, allowing study of the disconnected eddies. Algorithms employing contour surgery are available for this purpose (Dritschel 1988), however, we have chosen to limit the scope of the present study to times preceding the 'catastrophe' of the initial detachment.

It is instructive to compare the eddies of figure 5 with the finite-amplitude states found in the numerical experiments of PECC (in which the potential vorticity jump is weaker at $y = L_2$ than at $y = L_1$). In the latter, the unstable waves tended to break at $y = L_2$ but not at $y = L_1$, resulting in filamentation and eddy detachment (see their

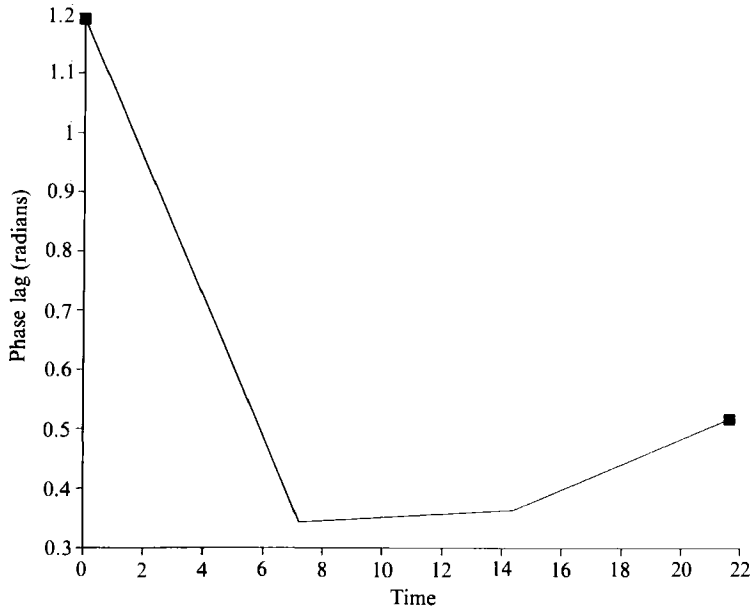

FIGURE 7. Phase lag θ_1 for the first Fourier mode of Run 1.

figures 13–15). A fundamental difference between this and the present case is that nonlinear long-wave steepening exists in the former. In the present case, where long-wave steepening is absent, their eddies are generated by pooling of the middle region, actual breaking (multivaluedness of L_1 and L_2) occurring very late in the course of evolution, only after the eddies have formed.

In order to obtain some measure of the frontal structure as the wave grows to large amplitude, we have Fourier decomposed the north front according to

$$L_1(x,t) = \tfrac{1}{2}\Delta L + A_1(t)\cos[\pi x/l + \theta_1] + A_2(t)\cos[2\pi x/l + \theta_2] + \ldots, \qquad (5.2)$$

with a similar expression for the south front. The length of the periodic domain is l and the amplitude and phase of the nth Fourier component are denoted by A_n and θ_n. The representation (5.2) is used only as long as L_1 remains single-valued.

Figure 6 shows the amplitude $A_1(t)$ of the Fourier component having wavelength l (in this case the linearly most unstable wavelength) and the amplitudes of the first two harmonics $A_2(t)$ and $A_3(t)$. As shown in the figure, the primary wave dominates with some generation of harmonics occurring.

The phase lag for the $n = 1$ Fourier mode, the value of θ_1 for the north front minus θ_1 for the south front, is initially 1.19 radians. This phase shift is necessary for the wave to extract kinetic energy from the mean flow. Figure 7 gives the phase lag for subsequent times, showing it to decrease but remain positive as the wave grows.

5.2. *Subharmonics* ($k = 1$ *and* $k = 0.5$)

The initial (or 'primary') wave of Run 2, $k = 1$, is the first subharmonic of the most unstable wave. The initial phase shift $\theta_1 = 0.45$ is smaller than that of the primary wave, indicating a stronger sinuous structure. The growth rate is roughly half the value for $k = 2$.

Since the primary wave will generate higher harmonics through nonlinear wave–wave interactions, Run 2 can be viewed as a competition experiment between the primary wave and its first harmonic (which grows more rapidly but has zero initial amplitude). As shown in figure 8, the overall evolution is similar to the

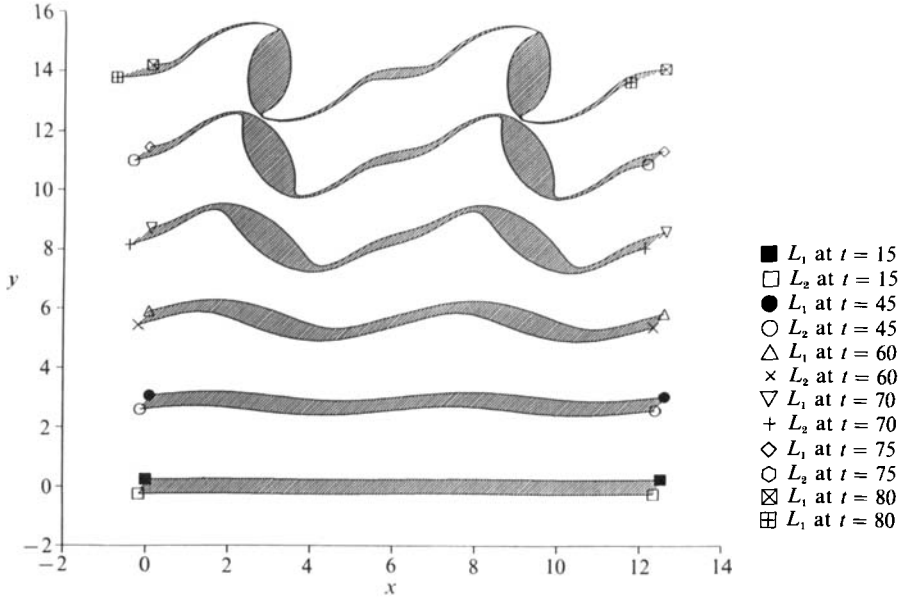

FIGURE 8. Run 2: $\Delta L = 0.5$, $k = 1$ (the first subharmonic of the most unstable wave). The solutions shown here are actually those of Run 2D, a high resolution repeat of Run 2.

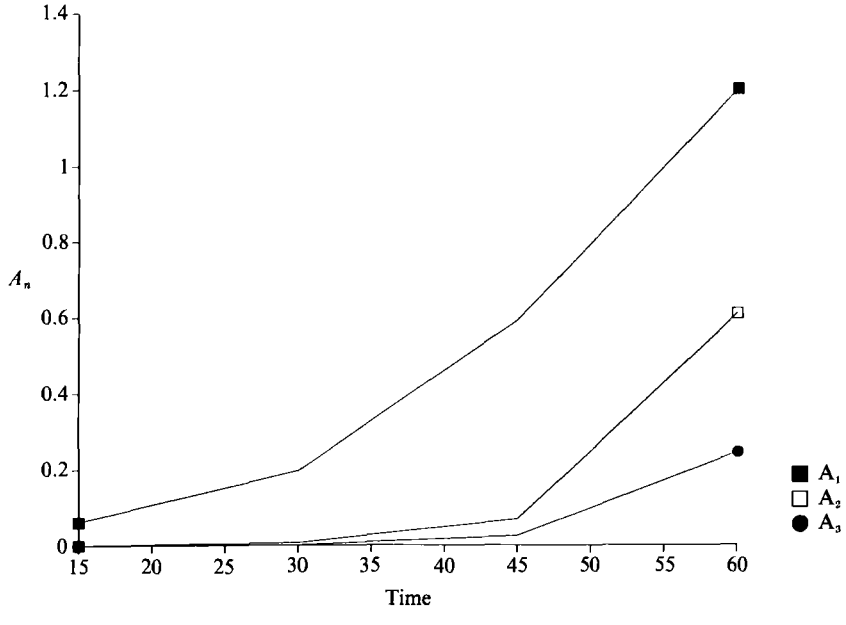

FIGURE 9. Fourier amplitudes A_1 (the primary wave), A_2 (its first harmonic, the linearly most unstable wave), and A_3 (the second harmonic) for Run 2.

previous case, the shaded fluid pooling into detaching eddies. The primary wave dominates in the sense that there is only one pool per primary wavelength. However, some evidence of the first harmonic is present, one indication being the secondary bulge forming at $t = 60$ near $x = 6$.

The Fourier amplitude A_1 for the primary wave and its first and second harmonics (A_2 and A_3) are shown in figure 9. The primary wave initially grows most rapidly owing to the fact that the higher harmonics have zero amplitude at $t = 0$. (According

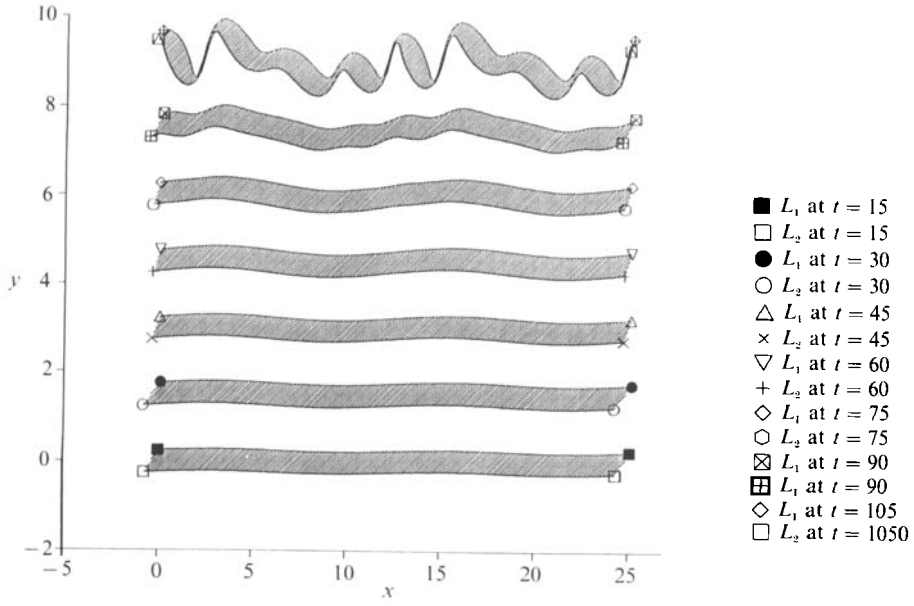

FIGURE 10. Run 4: $\Delta L = 0.5$, $k = 0.5$ (the second harmonic of the linearly most unstable wave).

to linear theory, the contribution to $\partial L/\partial t$ by the nth Fourier component is $A_n(0)\, kc_i \exp[kc_i t]$, and $A_2(0) = A_3(0) = 0$.) By $t = 50$, the first harmonic is growing more rapidly than the primary wave; however, a catastrophe (eddy detachment) occurs before the former can overtake the latter.

A strikingly different picture emerges when $k = 0.5$ is selected as the primary wavenumber (Run 4). The competition is now between this wave, its first harmonic ($k = 1.0$, the primary wave of the previous example) and its second harmonic ($k = 2.0$, the fastest growing wave). As shown in figure 10, the pools of shaded fluid are forming on a scale approximately a quarter of the primary wavelength (see the $t = 105$ frame). Modulation of the pooling process also occurs on a scale of half the primary wavelength. These pooling scales indicate influence of the fastest growing wave and its first subharmonic ($n = 3$ and $n = 2$).

Fourier analysis of L_1 for Run 4 indicates domination of the amplitude A_1 associated with the primary wavelength, as shown in figure 11. The amplitude A_3 associated with the most unstable wavelength reaches a third the value of A_1 by $t = 105$ and exceeds A_2 by only a small amount. The domination of $n = 3$ in the pooling process is a consequence of the lateral structure of the waves, as indicated by the north-to-south front phase shift (figure 12). The primary ($n = 1$) wave initially has a small ($\theta_0 = 0.2$) phase shift and this strong sinuous structure persists as the flow evolves, the $n = 2$ and $n = 3$ modes initially have large phase shifts ($\theta_2 = 0.45$ and $\theta_3 = 1.19$, respectively), indicating the stronger varicose component necessary for pooling. Although these phase shifts decrease at later times, they remain significantly larger than the $n = 1$ phase shift and the pooling thus occurs on the scales of $n = 2$ and $n = 3$.

These two calculations illustrate the importance of phase in determining the eddy spacing. Although waves with a small phase shift may be associated with the largest frontal excursions, as in the previous example, their strong sinuous structure rules out pooling. Instead, shorter waves with larger phase shifts are responsible for the pooling and the 'catastrophe' of eddy detachment.

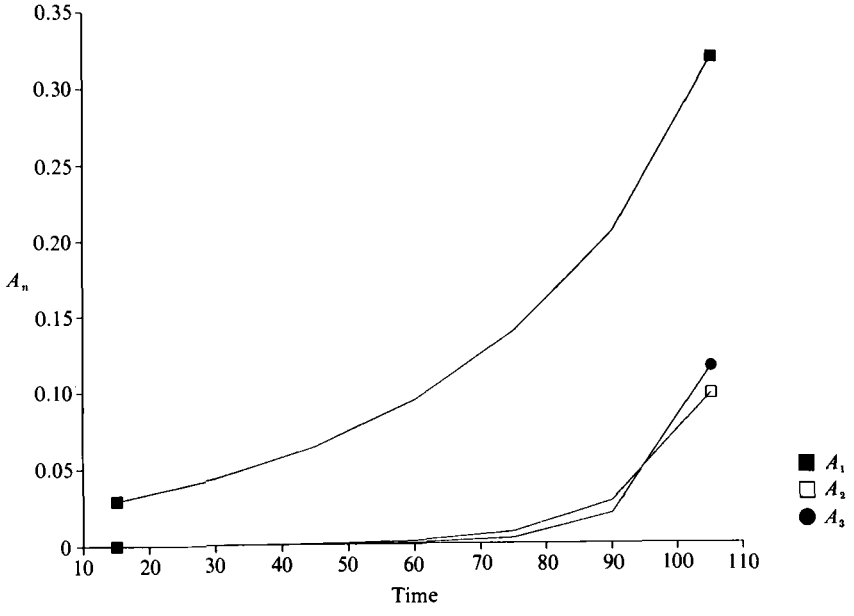

FIGURE 11. Fourier amplitudes A_1 (the primary wave), A_2 (its first harmonic), and A_3 (its second harmonic, the linearly most unstable wave) for Run 4.

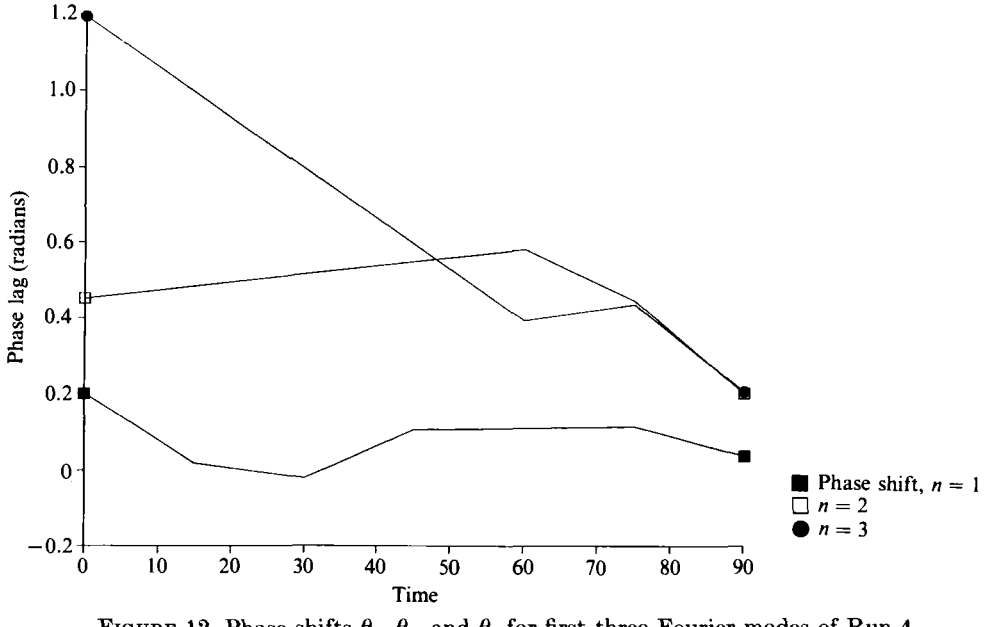

FIGURE 12. Phase shifts θ_1, θ_2, and θ_3 for first three Fourier modes of Run 4.

5.3. *Competition experiment*

A further demonstration of the importance of phase in determining the shape and spacing of the eddies can be made by initiating a competition experiment between two waves having equal growth rate. In this case the initial condition is given by

$$L_1 = \tfrac{1}{2}\Delta L + 0.02\sin(k_1 x) + 0.02\sin(k_2 x + \theta_0),$$
$$L_2 = -\tfrac{1}{2}\Delta L + 0.02\sin(k_1 x + \theta_1) + 0.02\sin(k_2 x + \theta_2 + \theta_0),$$

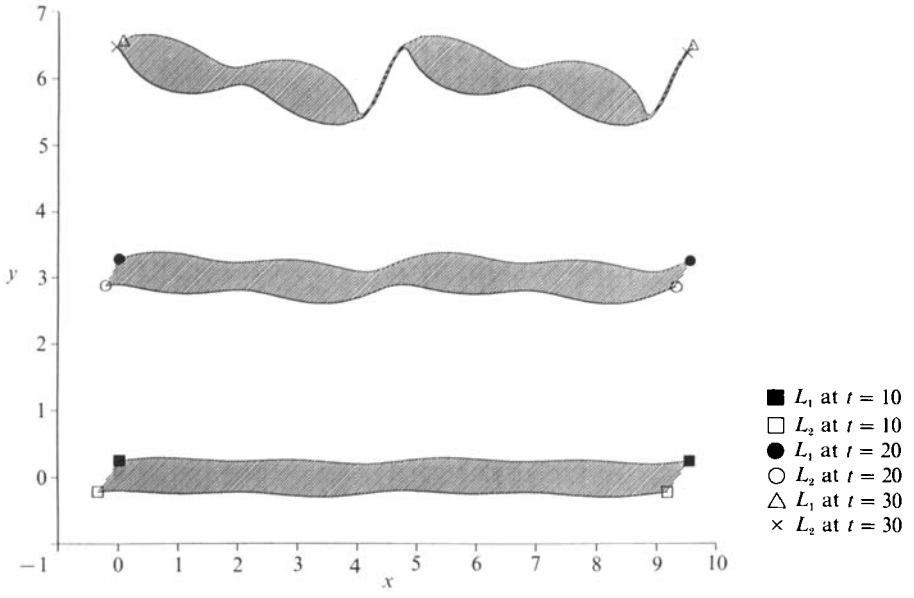

FIGURE 13. Competition experiment between $k_1 = 1.31$ and $k_2 = 2.62$ with $\Delta L = 0.5$ (Run 5). Both waves have the same linear growth rate $kc_i = 0.105$.

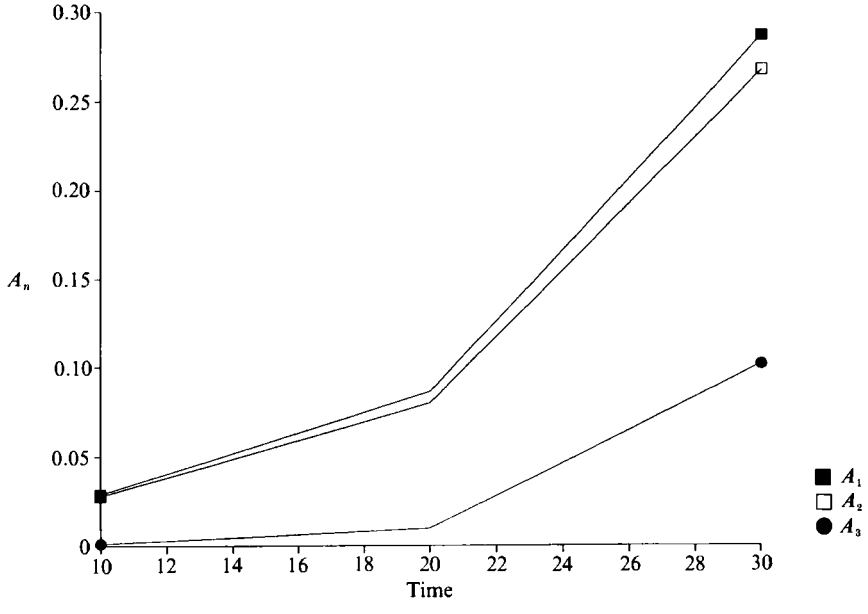

FIGURE 14. Fourier amplitudes A_1 ($k = 1.31$) and A_2 ($k = 2.62$) for the two primary waves of Run 5.

choosing $k_1 = 1.31$ and $k_2 = 2.62$, with corresponding phase shifts $\theta_1 = 0.642$ and $\theta_2 = 2.00$, gives two waves having the same growth rate (e-folding time = 9.54).

The phase shift θ_0 of the first wave relative to the second is set to zero for the first case (Run 5, figure 13). Evidence of both wavelengths is present in the pooling occurring at $t = 30$. The Fourier amplitudes A_1 and A_2 for k_1 and k_2 remain approximately equal as the flow evolves (figure 14) but the phase shift for k_1 remains substantially less than that for k_2 (figure 15). In other words, there is little energy

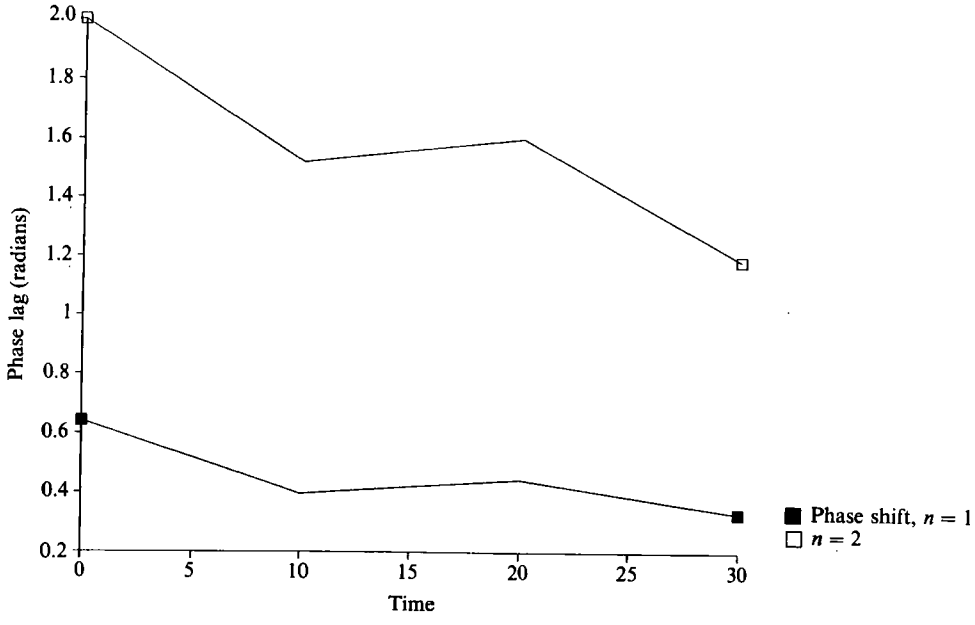

FIGURE 15. Phase shifts θ_1 and θ_2 for the primary waves of Run 5.

exchange between the two waves, and it is the stronger phase structure of the second wave that allows it, rather than the first, to determine the pool spacing.

It is also instructive to vary the phase lag θ_0 of the first wave relative to the second. In Run 5a (figure 16), we have set $\theta_0 = \pi$, so that the crests of the second (k_2) wave are displaced by half its wavelength relative to the first example. The Fourier amplitudes and phase shifts for this case (not shown) are similar to those at Run 5 and pools again form at the spacing $2\pi/k_2$ (figure 16). However, the orientation and staggering of the pools differs markedly from the previous case (figure 13).

5.4. *Weakly nonlinear case*

Continuing with initial conditions of the type (5.1), we now consider the setting $k = 2.9$ lying just within the short-wave cutoff ($k = 3.0$). This weakly unstable wave has a strong varicose structure ($\theta_1 = 0.91\pi$) and should be governed at early times by the weak nonlinear theory (§4).

As shown in figure 17, the flow develops into a series of detached eddies spaced at the primary wavelength. Since subharmonics of the primary wave are eliminated by the periodic boundary conditions, no faster growing linear modes are present. The detachment process begins at about $t = 80$, or about two and a half e-folding times. According to (4.19) the time t_s required for the amplitudes to become infinite is about three e-folding times.

The significance of these findings is that the flow is nonlinearly unstable (as predicted), that the qualitative nature of the catastrophe remains the same as in early calculations and that the catastrophe time is comparable to t_s.

5.5. *Experiments with stabilized intermediate conditions*

We have seen that certain features of the finite-amplitude state such as the pool spacing can be explained using properties of the linearly unstable waves. One might ask whether the linear instability remains essential to the growth and evolution of

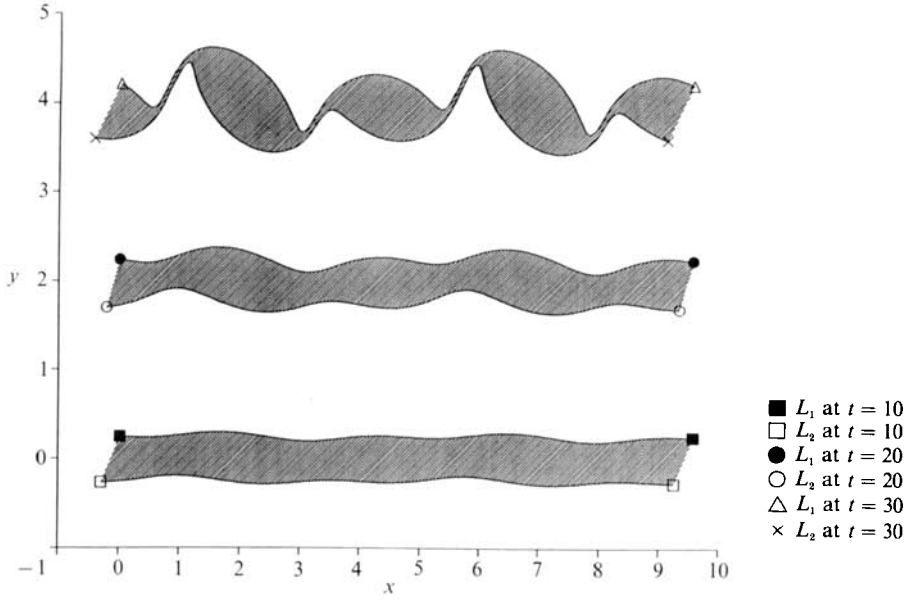

FIGURE 16. Run 5a: identical to Run 5 except that the two primary waves have been phase shifted an amount $\theta_0 = \pi$ in the x-direction.

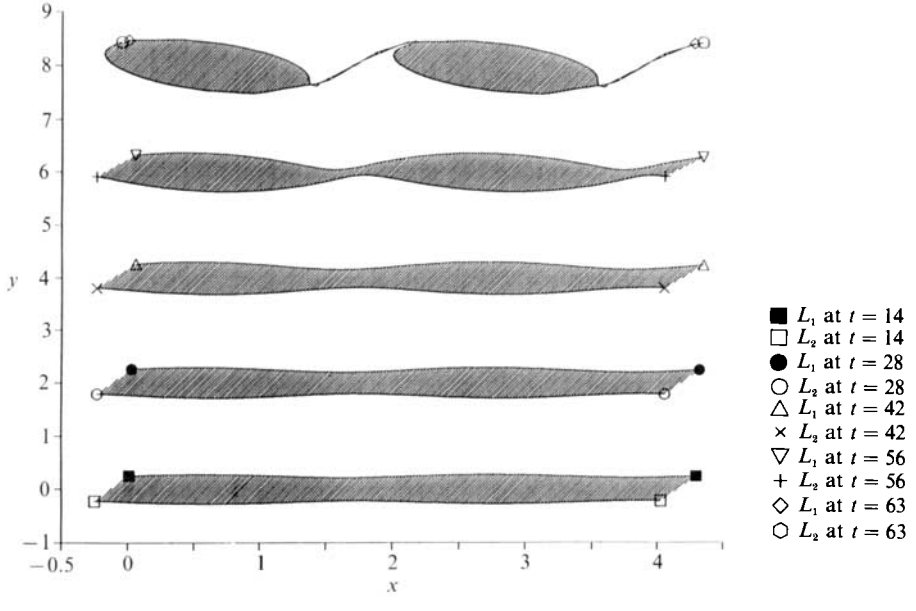

FIGURE 17. Run 3c: $\Delta L = 0.5$, $k = 2.9$ (marginally unstable wave).

the finite amplitude states or whether growth and pooling is due entirely to nonlinear dynamics on a scale preset by the linear instability.

Reconsider Run 3 (figure 17), which satisfies the weak growth condition required by the finite-amplitude theory of §4. At $t = 42$, we interrupt the time integration and multiply L_1 and L_2 by factor 1.04, a procedure equivalent to decreasing the deformation radius by factor 1/1.04. For the primary wavenumber $k = 2.9$ this distortion is sufficient to linearly stabilize the flow; that is, wavenumber $k = 2.9$ is

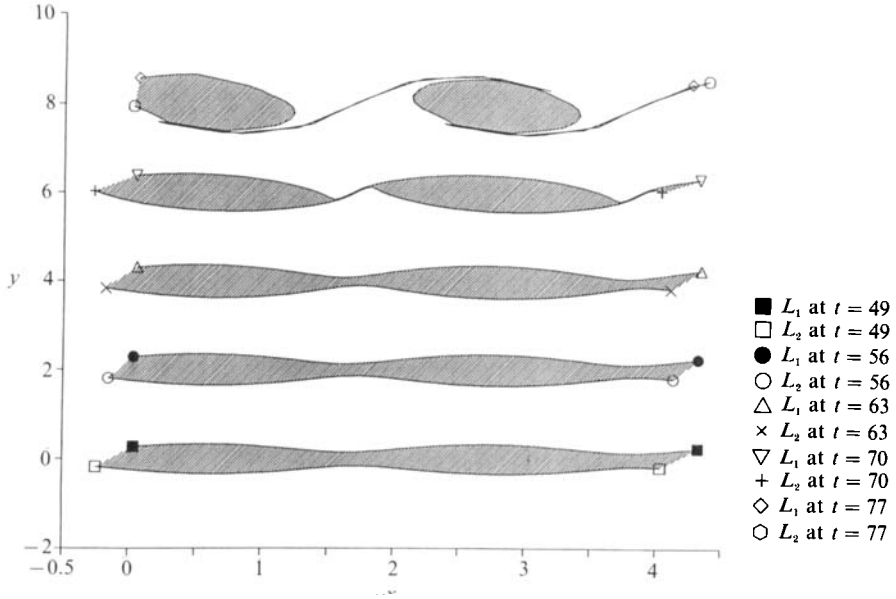

FIGURE 18. Run 3d: The initial condition is the same as Run 3c, however L_1 and L_2 are magnified by factor 1.04 at $t = 49$.

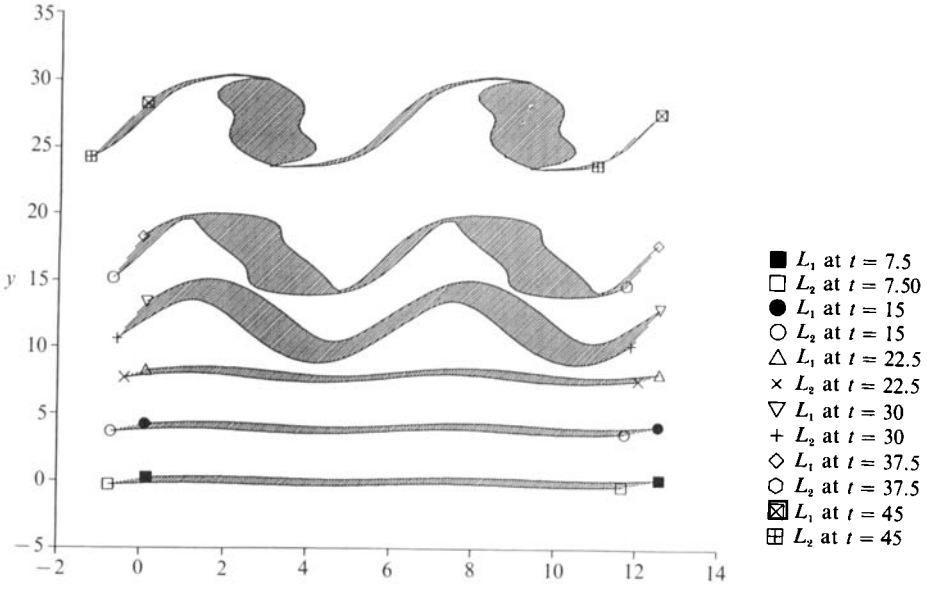

FIGURE 19. Run 2b: The initial conditions are identical to those of Run 2 (figure 8). At $t = 30$, L_1 and L_2 are magnified by factor 4.0.

stable in a basic flow having $\Delta L = 1.04 \times 0.5$. Figure 18 shows the subsequent evolution, beginning at $t = 49$. Although eddy detachment takes a bit longer ($t_p \approx 70$ as opposed to $t_p \approx 63$), the overall picture remains the same, indicating the dominance of nonlinearity in the growth and eventual pooling.

The dominance of nonlinear terms at later times could have been anticipated on the basis of the amplitude evolution equation. As $|A|$ grows the nonlinear term, being cubic, eventually dominates the linear term.

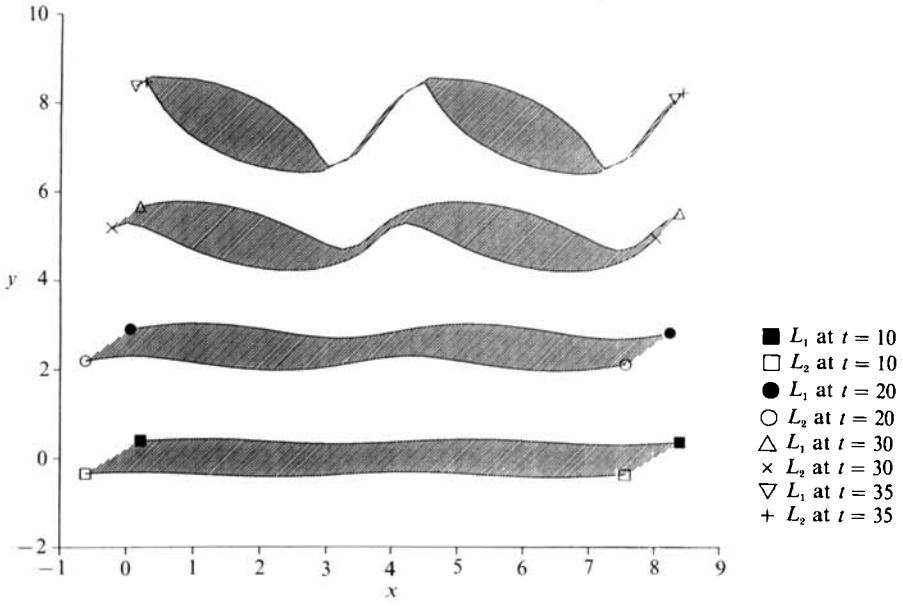

FIGURE 20. Run 7: $\Delta L = 0.75$, $k = 1.5$ (the linearly most unstable wave).

A similar procedure was applied to Run 2 (figure 8). The values of L_1 and L_2 were amplified by factor 4.0 at $t = 30$, barely enough to linearly stabilize the basic state at the primary wavenumber. The evolution of this highly distorted state (figure 19) is qualitatively similar to that of figure 8, with the major pools spaced at the primary wavelength and a secondary bulge forming near $x = 6$. The pools do differ in shape, higher wavenumber distortion appearing in figure 19. Although these differences may ultimately become important, the qualitative evolution from $t = 30$ to the initial catastrophe is due primarily to nonlinear dynamics.

5.6. *Other values of* ΔL

To determine whether the nature of the finite amplitude states remains qualitatively the same at different values of ΔL, Runs 6 ($\Delta L = 0.25$) and 7 ($\Delta L = 0.75$) were carried out. In each case, the values of k and θ_0 for the most unstable linear wave was chosen. Figure 20 shows the result for the case $\Delta L = 0.75$. For this case and Run 6 (not shown), pools form at the primary wavelength in a manner similar to previous cases.

5.7. *Catastrophe time*

According to weakly nonlinear theory, the excursions of the fronts become infinite at a finite time t_s. Since the frontal displacement η has been scaled by the small parameter ϵ, the distance ΔL between fronts is essentially seen as infinite by the growing wave, and one might expect t_s to approximate the time t_p required for contact to occur between fronts. Since the weakly nonlinear theory is formally valid for marginally unstable waves, the most reasonable test of this idea is based on Run 3c, for which the primary wave is slightly supercritical. For the initial amplitude used in this case, t_s is about 2.7 e-folding times. The observed pinch-off time $t \approx 63$ (table 1) is about 1.8 e-folding times. Thus weak nonlinear theory provides a timescale which moderately overestimates t_p.

In Runs 1, 2, 6, and 7, the eddies develop from growth of the primary wave. The initial amplitude for these runs is identical to Run 3c. These conditions are similar

to those realized in Run 3c, and the values of t_s range from 3.1 to 4.1 e-folding times. For Runs 5 and 5a, which involved two primary waves having identical growth rate, t_s was 3.1 e-folding times. In each case, weakly nonlinear theory appears to provide a reasonable estimate for the scale of t_s.

5.8. *Necessary condition for finite-amplitude instability*

Dritschel (1988) has recently derived bounds on the mean displacements of potential vorticity contours from their undisturbed positions. For the two-front system discussed by PECC, the displacements η_1 and η_2 of the two fronts about their equilibrium positions are restricted by

$$\int_0^\lambda (\Delta Q_1 \eta_1^2 + \Delta Q_2 \eta_2^2)\, dx = \text{constant},$$

where ΔQ_n denotes the potential vorticity jump across $y = L_n$ and λ the length of the periodic domain. This constraint can be viewed as a necessary condition for instability, valid for large displacements of the fronts. The flow can be unstable (in the sense that the mean square displacements of both fronts increase with time) only if ΔQ_1 and ΔQ_2 have opposite signs. This necessary condition is satisfied in the present model (for which $\Delta Q_1 = -\Delta Q_2$) and is consistent with the observed amplitude.

6. Conclusions

It is now clear that instability can produce detached eddies or pools without the aid of nonlinear long-wave steepening. In fact, no cases have been found in which the linear instability fails to produce a train of pools, a result supported by our weakly nonlinear analysis predicting nonlinear instability for marginally unstable waves at all values of ΔL. The explosive nonlinear instability seems to be a feature of other waves as well. When we interrupt the numerical runs at moderate amplitude and 'linearly stabilize' the flow, the dominance of nonlinear dynamics is asserted by a subsequent evolution qualitatively similar to the uninterrupted case.

One's ability to predict the spacing and detachment time t_p for the pools is somewhat dependent on the initial conditions. In runs where a single primary wave is present, the pools are normally spaced at the primary wavelength and t_p is approximated by the weakly nonlinear catastrophe time t_s. Exceptions can occur when the primary wavenumber lies far enough to the left of the maximum in the growth rate curve. In such cases, a harmonic of the primary wave may dominate the pooling process, relying on its stronger varicose phase structure. The only example considered here, Run 4, has a pool spacing of quarter of the primary wavelength. Somewhat surprisingly, the value of t_p (2.69 times the e-folding time) is almost exactly equal to t_s ($= 2.70$). In competition experiments involving two primary waves of equal linear growth rates, the wave with the strongest varicose phase structure determines the pool spacing.

Logical extensions of the present work include consideration of unequal potential vorticity jumps (i.e. the jump ratio $r \neq 1$ in the equations of PECC). For $0.2 \leqslant r \leqslant 0.6$, a range argued by PECC to be appropriate to the Gulf Stream, the basic flow takes the form of a jet. Although this flow is linearly unstable, it is not known whether the explosive nonlinear instability is present and, if so, whether it is restricted to certain ranges in ΔL. A second obvious and important extension is to the case of an active lower layer.

The authors gratefully acknowledge the support of the National Science Foundation under grants OCE 87-00601 and ATM 89-03890 and the Office of Naval Research under grant N00014-89-K-1182. We would also like to thank Anne-Marie Michael for preparing the manuscript.

Appendix A

The numerical procedure used to integrate equations (2.9*a–d*) is adapted from the one described in Appendix A of PECC. The PECC algorithm is designed for an isolated disturbance and can be adapted to the present periodic domain by making the following substitutions. In their equations (A 2) and (A 3), the terms $I_1^{(1)}$, $I_2^{(1)}$, $I_4^{(2)}$, and $I_5^{(2)}$ should be replaced by

$$I_1^{(1)} = \frac{1}{2}\sum_{l=1}^{N}\sum_{j=2}^{n}(x_j^{(1)}-x_{j-1}^{(1)})\{K_0[R_i^{(1)}(x_j^{(1)}-l\cdot\gamma)]+K_0[R_i^{(1)}(x_{j-1}^{(1)}-l\cdot\gamma)]\},$$

$$I_2^{(1)} = \frac{1}{2}\sum_{l=-1}^{-N}\sum_{j=2}^{n}(x_j^{(1)}-x_{j-1}^{(1)})\{K_0[R_i^{(1)}(x_j^{(1)}-l\cdot\gamma)]+K_0[R_i^{(1)}(x_{j-1}^{(1)}-l\cdot\gamma)]\},$$

$$I_4^{(2)} = \frac{1}{2}\sum_{l=1}^{N}\sum_{j=2}^{n}(x_j^{(2)}-x_{j-1}^{(2)})\{K_0[R_i^{(2)}(x_j^{(2)}-l\cdot\gamma)]+K_0[R_i^{(2)}(x_{j-1}^{(2)}-l\cdot\gamma)]\},$$

$$I_5^{(2)} = \frac{1}{2}\sum_{l=-1}^{-N}\sum_{j=2}^{n}(x_j^{(2)}-x_{j-1}^{(2)})\{K_0[R_i^{(2)}(x_j^{(2)}-l\cdot\gamma)]+K_0[R_i^{(2)}(x_{j-1}^{(2)}-l\cdot\gamma)]\}.$$

In addition, the terms $I_5^{(1)}$, $I_6^{(1)}$, $I_1^{(2)}$, and $I_2^{(2)}$ should be replaced by

$$I_5^{(1)} = \frac{1}{2}\sum_{l=1}^{N}\sum_{j=2}^{n}(x_j^{(2)}-x_{j-1}^{(2)})\{K_0[R_i^{(1)}(x_j^{(2)}-l\cdot\gamma)]+K_0[R_i^{(1)}(x_{j-1}^{(2)}-l\cdot\gamma)]\},$$

$$I_6^{(1)} = \frac{1}{2}\sum_{l=-1}^{-N}\sum_{j=2}^{n}(x_j^{(2)}-x_{j-1}^{(2)})\{K_0[R_i^{(1)}(x_j^{(2)}-l\cdot\gamma)]+K_0[R_i^{(1)}(x_{j-1}^{(2)}-l\cdot\gamma)]\},$$

$$I_1^{(2)} = \frac{1}{2}\sum_{l=1}^{N}\sum_{j=2}^{n}(x_j^{(1)}-x_{j-1}^{(1)})\{K_0[R_i^{(2)}(x_j^{(1)}-l\cdot\gamma)]+K_0[R_i^{(2)}(x_{j-1}^{(1)}-l\cdot\gamma)]\},$$

$$I_2^{(2)} = \frac{1}{2}\sum_{l=-1}^{-N}\sum_{j=2}^{n}(x_j^{(1)}-x_{j-1}^{(1)})\{K_0[R_i^{(2)}(x_j^{(1)}-l\cdot\gamma)]+K_0[R_i^{(2)}(x_{j-1}^{(1)}-l\cdot\gamma)]\}.$$

These terms approximate the contour integrals in (2.9) over the periodic domains neighbouring the primary domain. The quantity N is the number of periodic intervals resolved on either side of the primary interval. In the numerical runs performed here $N = 3$. All other notation is defined in PECC.

The number n of Lagrangian points per periodic interval is kept constant in each run, although the points are periodically redistributed such that higher resolution is imposed in areas of high curvature. The point redistribution scheme is described in PECC. Values of n for each run are given in table 1.

Numerical accuracy tests were performed using the initial condition specified by Run 1 in table 1. With $NP = 40$, the initial growth rate differed from the value predicted by linear theory by only 2%. Runs with variable resolution were also performed (see Runs 2c and 3d in table 1) and the changes in resolution were not found to yield qualitative changes in the solution. The only exception occurs when

the initial wave is marginally unstable, as in Run 3. In this case, insufficient resolution can prevent the wave from growing (see Runs 3a and 3d in table 1). Other accuracy tests are described in PECC.

Appendix B

The constants C_1 and C_2, which appear in the amplitude evolution equation (4.20), are derived by the orthogonality condition described in §4. They are

$$C_1 = \frac{1}{\mu} e^{-2\mu}\left[\frac{\kappa_0}{\sinh^2\kappa_0} + \frac{\kappa_0}{\mu} + \frac{\kappa_0}{\cosh^2\mu} + \frac{\kappa_0 \tanh\mu}{\mu} - (1+\coth\mu)\right], \tag{B 1}$$

$$C_2 = \frac{4e^{2\mu}}{\mu \sinh^2 2\mu}[\bar{X}_1 + \bar{X}_2 + \bar{X}_3], \tag{B 2}$$

where

$$\bar{X}_1 = (\kappa_0 - 2\mu)\{\kappa_0\mu(1-\coth\kappa_0\tanh\mu) - \kappa_0^2(1-\coth^2\kappa_0)\} - \kappa_0\gamma^2(1+\coth\kappa_0), \tag{B 3a}$$

$$\bar{X}_2 = [\kappa_0\gamma(1-\coth\kappa_0\tanh\gamma) + \kappa_0\mu(1-\coth\kappa_0\tanh\mu) - \kappa_0^2(1-\coth^2\kappa_0) - \kappa_0(\kappa_0-\mu)(1+\coth\kappa_0)] \times \frac{[\mu^2/(\coth^2\mu) + \mu(\gamma-\kappa_0)(1+\tanh\mu)]}{\mu(1+\tanh\mu) - \gamma(1+\tanh\gamma)}, \tag{B 3b}$$

$$\bar{X}_3 = \kappa_0(1+\coth\kappa_0)[\kappa_0\gamma + \kappa_0\mu(1-\coth\kappa_0\tanh\mu) - \kappa_0^2(1-\coth^2\kappa_0) - (\kappa_0-\mu)\{2(\kappa_0-\mu) + \kappa_0\coth\kappa_0\}]. \tag{B 3c}$$

The coefficient C_1 may be independently derived (and hence the machinery of the calculation subjected to unification) by expanding the expression for the phase speed C, given by linear theory, around the neutral point, viz.

$$\frac{C^2}{U^2} = \frac{\sinh 2\mu\, e^{-2\mu}}{2\mu^2}\left[-\frac{\mu^2}{\sinh^2 2\mu} + \{\mu(1+\coth 2\mu) - \kappa(1+\coth\kappa)\}^2\right], \tag{B 4}$$

where $\mu^2 = \kappa^2 + k^2$.

At the neutral point $\kappa = \kappa_0$ and μ is related to κ_0 by (4.17). The expansion of (B 4) for $\kappa = \kappa_0 + \delta\kappa$ will yield

$$C_1 = -\frac{1}{U^2}\left(\frac{\partial C^2}{\partial\kappa}\right)_{\kappa=\kappa_0}. \tag{B 5}$$

The coefficient of the cubic term in A in the amplitude equation can only be attained by the perturbation method described in §4. As noted above, it is a very complicated function of the parameters κ_0 and k. We have each independently calculated C_2 to minimize the possibility of algebraic error. The result for C_2 is at least consistent with the behaviour of the perturbation evolution obtained by our contour dynamical calculations.

REFERENCES

Armi, L. 1989 Hydraulic control of zonal currents on a β-plane. *J. Fluid Mech.* **201**, 357–377.

Byrd, P. F. & Friedman, M. D. 1971 *Handbook of Elliptic Integrals for Engineers and Scientists*, pp. 359. Springer.

Cornillon, P., Evans, D. & Large, W. 1986 Warm outbreaks of the Gulf Stream into the Sargasso Sea. *J. Geophys. Res.* **91**, 6583–6596.

DRITSCHEL, D. 1988 Contour surgery: a topological reconnection scheme for extended integrations using contour dynamics. *J. Comput. Phys.* **77**, 240–266.

FLIERL, G. R. & ROBINSON, A. R. 1984 On the time dependent meandering of a thin jet. *J. Phys. Oceanogr.* **14**, 412–423.

GRIFFITHS, R. W., KILLWORTH, P. D. & STERN, M. E. 1981 Ageostrophic instability of ocean currents. *J. Fluid Mech.* **117**, 343–377.

PEDLOSKY, J. 1990 On the propagation of velocity discontinuities on potential vorticity fronts. *J. Phys. Oceanogr.* **20**, 235–240.

PRATT, L. J. 1988 Meandering and eddy detachment according to a simple (looking) path equation. *J. Phys. Oceanogr.* **18**, 1627–1640.

PRATT, L. J. 1989 Critical control of zonal jets of bottom topography. *J. Mar. Res.* **47**, 111–130.

PRATT, L. J., EARLES, J., CORNILLON, P. & CAYLULA, J.-F. 1990 The nonlinear behavior of varicose disturbances in a simple model of the Gulf Stream. *Deep-sea Res.* (in press).

RICHARDSON, P. L. 1983 Gulf Stream rings. In *Eddies and Marine Science* (ed. A. R. Robinson), pp. 19–45. Springer.

TALLEY, L. D. 1983*a* Radiating instabilities of thin baroclinic jets. *J. Phys. Oceanogr.* **13**, 2161–2181.

TALLEY, L. D. 1983*b* Radiating barotropic instability. *J. Phys. Oceanogr.* **13**, 972–987.

WARREN, B. A. & OWENS, W. B. 1988 Deep currents in the Central Subarctic Pacific Ocean. *J. Phys. Oceanogr.* **18**, 529–551.

ZABUSKY, N. J. & OVERMAN, E. A. 1981 Regularization of contour dynamical algorithms. *J. Comput. Phys.* **30**, 96–106.